Eur. Phys. J. Special Topics **222**, 569–585 (2013)

DOI: 10.1140/epjst/e2013-01860-9

THE EUROPEAN PHYSICAL JOURNAL SPECIAL TOPICS

Regular Article

Ordinal patterns in epileptic brains: Analysis of intracranial EEG and simultaneous EEG-fMRI

C. Rummel[1,a], E. Abela[1,2], M. Hauf[1,3], R. Wiest[1], and K. Schindler[2]

[1] Support Center for Advanced Neuroimaging, University Institute for Diagnostic and Interventional Neuroradiology, Inselspital, Bern University Hospital and University of Bern, Switzerland
[2] Department of Neurology, Inselspital, Bern University Hospital and University of Bern, Switzerland
[3] Klinik Bethesda Tschugg, Switzerland

Received 27 March 2013 / Received in final form 25 April 2013
Published online 25 June 2013

Abstract. Epileptic seizures are associated with high behavioral stereotypy of the patients. In the EEG of epilepsy patients characteristic signal patterns can be found during and between seizures. Here we use ordinal patterns to analyze EEGs of epilepsy patients and quantify the degree of signal determinism. Besides relative signal redundancy and the fraction of forbidden patterns we introduce the fraction of underrepresented patterns as a new measure. Using the logistic map, parameter scans are performed to explore the sensitivity of the measures to signal determinism. Thereafter, application is made to two types of EEGs recorded in two epilepsy patients. Intracranial EEG shows pronounced determinism peaks during seizures. Finally, we demonstrate that ordinal patterns may be useful for improving analysis of noninvasive simultaneous EEG-fMRI.

1 Introduction

Epilepsy is one of the most prevalent chronic neurological disorders with an estimated number of at least 50 million patients worldwide [1]. It is defined by the "enduring predisposition to generate epileptic seizures", which occur transiently "due to abnormal excessive or synchronous activity of the brain" [2]. These definitions of the International League Against Epilepsy (ILAE) and the International Bureau of Epilepsy (IBE) are remarkable because they not only encompass signs and symptoms of a neurological disorder but also "the neurobiologic, cognitive, psychological and social consequences" for the patients. One of the most disabling features of epilepsy is the unexpected occurrence of seizures. Despite considerable effort in the last 15 years they are still not reliably predictable [3,4] and meanwhile there is reasonable skepticism that they will ever be. Morbidity and mortality of epilepsy patients is increased [5] with seizure associated injury and death as important factors. Therefore, the prime goal of epilepsy therapy is seizure freedom. The challenge of current epileptology is

[a] e-mail: crummel@web.de

Fig. 1. Examples of representative intracranial EEG signals as identified by visual inspection. A) epileptic spike, B) focal slowing, C) low-voltage fast activity.

that despite up-to-date treatment still one out of four patients continues to suffer from epileptic seizures [6,7].

Electroencephalography (EEG) is still the key tool used in diagnosis, treatment planning and treatment control of epilepsy. Classic EEG analysis consists in visual inspection of the raw or minimally pre-processed multi-channel time series by trained clinical experts. In this analysis, pattern recognition and the notion of "grapho elements" (i.e. typical EEG patterns that are associated with certain disorders) play a fundamental role. For illustration we show in Fig. 1 a selection of three EEG patterns that are associated with epilepsy. An *epileptic spike* (panel a) has typically a large amplitude relative to the background activity, occurs suddenly, is pointed and asymmetric, i.e. increases faster than it decreases and is followed by a slow wave [8]. It has long been thought that the spike is due to "excessive and hypersynchronous" discharges of neurons, and the slow wave due to recurrent inhibition. However a recent study implies that this assumption may be too simplistic [9]. Panel b shows an instance of *focal slowing* as may be recorded from cortical regions that are pathologically altered. Note that generalized slowing physiologically occurs during deepening sleep. *Low-voltage fast activity* (panel c) recorded at the onset of a focal seizure is an excellent biomarker for epileptogenic brain areas.

Nowadays visual EEG reading is increasingly complemented by quantitative EEG (qEEG) analysis, see e.g. [10–13] for reviews. In qEEG analysis methods of linear or nonlinear, uni-, bi- or multivariate time series analysis [14,15] are used to characterize the signals. Here, we concentrate on recent developments using ordinal patterns for univariate, nonlinear qEEG analysis. Ordinal patterns are defined by all possible relative orderings of neighboring signal values and offer a coarse grained view of the underlying dynamics. For application to EEG time series, similarities with visual EEG reading have recently been pointed out [16]. Both, visual and ordinal pattern based EEG analysis, classify the signals by the temporal sequence of amplitude values. In the first case regular ("rhythmic", "monomorphic") EEG signals are differentiated from more variable ("pleomorphic") ones. In ordinal pattern analysis something similar is achieved in a mathematically more rigorous way by mapping amplitude sequences to a finite number of possible patterns. A difference between both approaches is the time scale, on which analysis is applied. While in visual EEG reading the typical time scale is seconds, ordinal pattern analysis is applied for neighboring signal samples (occasionally with delays of a small number of samples). The latter sets the typical time scale to tens of milliseconds.

Apart from very special dynamical maps [17], a generally accepted rule of thumb is that the more random the dynamics of a system is, the more different ordinal patterns are generated. Vice versa, the more deterministic the dynamics is, the less different ordinal patterns normally occur [18]. We here use scalar quantifiers for the distribution of EEG derived ordinal patterns as measures for signal determinism. The search for increased or reduced determinism in certain time periods or brain regions is motivated by the finding that on the behavioral level epileptic seizures evolve very stereotypically. The question arises whether brain areas showing increased determinism play a particular role in seizure initiation, propagation or termination.

Besides the non-occurring ordinal patterns, also referred to as *"missing"* or *"forbidden ordinal patterns"*, we here study *"under-represented patterns"* and the signal's *"relative redundancy"*. After the seminal paper by Bandt and Pompe [19] that introduced the concept of *"permutation entropy"* for analysis of temporal relationships in time series several applications of ordinal pattern-based analysis methods were used to study ictal (i.e. during seizures) surface EEG [20–22] and intracranially recorded local field potentials in a rat model of absence seizures [23]. Human peri-ictal intracranial EEG was analyzed in [16,24]. A recent review on applications in bio-medicine and econophysics was published in [25].

In the present contribution we compare the performance of three quantifiers for ordinal pattern distributions at the example of the logistic map with superimposed noise. We present parameter scans and discuss the sensitivity to signal determinism. Then, application is made to qualitatively different EEG types of two patients who underwent surgical epilepsy therapy. The first type is highly invasive intracranial EEG (iEEG) that is directly recorded from electrodes implanted inside the head and offers very high spatial resolution and signal-to-noise ratio (SNR), see e.g. [7,26] for reviews. The second type is EEG recorded simultaneously with functional magnetic resonance imaging (fMRI), see e.g. [27–29]. This technique allows non-invasive localization of the brain regions where interictal epileptic discharges (IEDs) are generated.

2 Quantifiers for ordinal pattern distributions and signal determinism

To map a time series x_t with $t = 1, \ldots, L$ to a finite number of ordinal patterns we first choose two parameters, a pattern order $d > 1$ and a time delay $\tau \geq 1$. Then d observations x_t spaced at τ sample times are picked to generate an embedding (row) vector of dimension d:

$$\mathbf{x}_s = (x_s, x_{s+\tau}, \ldots, x_{s+(d-1)\tau}). \tag{1}$$

The elements of the vector $\mathbf{x}_s$ are mapped uniquely onto the permutation $\boldsymbol{\pi} = (\pi_0, \pi_1, \ldots, \pi_{d-1})$ of $(0, 1, \ldots, d-1)$ that fulfills

$$x_{s+\pi_0\tau} \leq x_{s+\pi_1\tau} \leq \ldots \leq x_{s+\pi_{d-1}\tau} \ . \tag{2}$$

Equal values are uniquely ordered in the time of their appearance in $\mathbf{x}_s$. As an example, the 5-dimensional embedding vector $\mathbf{x}_s = (1.26, 6.38, 0.63, 1.26, 4.92)$ is mapped onto the ordinal pattern $\boldsymbol{\pi} = (2, 0, 3, 4, 1)$.

In dimension d there are in total $d!$ different permutations $\boldsymbol{\pi}$. Different initial samples x_s in general lead to different embedding vectors $\mathbf{x}_s$ and different ordinal patterns $\boldsymbol{\pi}$. The sample size of ordinal patterns generated from a time series of length L is $N = L - (d-1)\tau$.

2.1 Inequalities

In principle, d and τ are free parameters. However, in order to sample the empirical distribution of ordinal patterns densely enough for reliable estimation of its probability density we require the following condition [30,31] for the "sample size ratio":

$$\mathrm{SSR} = N/d! \gg 1. \tag{3}$$

In addition, for real world time series the parameters d and τ are subject to restrictions in terms of the period $T_{\min} = 1/f_{\max}$ of the highest frequency present in the data.

Patterns of order d and delay τ cover a segment of length $l = (d-1)\tau + 1$ of the time series x_t, which reduces to $l = d$ for the prominent case $\tau = 1$. Measuring l and τ in time units, we propose to require:

$$l > T_{\min} > 2\tau. \tag{4}$$

Neglecting 1 against $(d-1)\tau$ this simplifies to

$$d - 1 \gtrsim T_{\min}/\tau > 2. \tag{5}$$

Violation of the left inequality in Eqs. (4) and (5) introduces a bias that may underestimate the importance of non-oscillating patterns. The right inequality prevents from aliasing problems (i.e. the phenomenon that high frequency oscillations could mimic low frequency variations).

2.2 Permutation entropy and relative redundancy

In [19] *"permutation entropy"* has been introduced as a scalar quantifier for a distribution of N ordinal patterns:

$$H = -\sum_{i=1}^{d!} p_i \cdot \log(p_i). \tag{6}$$

Here, the p_i are the probabilities of the patterns "i". Empirically the permutation entropy is estimated from

$$h = -\sum_{i=1}^{d!} \frac{n_i}{N} \cdot \log\left(\frac{n_i}{N}\right), \tag{7}$$

where the n_i are the empirical pattern frequencies with $\sum_i n_i = N$. To be independent from the pattern order d we here report the *"relative redundancy"* or *"normalized Kullback-Leibler entropy"* [32], which is defined as one minus the normalized permutation entropy:

$$r = 1 - \frac{h}{\log(d!)}. \tag{8}$$

The relative redundancy assumes values in the interval $[0, 1]$ with $r = 0$ for a uniform pattern frequency distribution $n_i \equiv N/d!$ and $r = 1$ if only one pattern is present: $n_i = N$ and $n_{j\neq i} = 0$. Based on bit strings instead of ordinal patterns application of the relative redundancy to human intracranial EEG has been made in [24].

2.3 Fraction of forbidden and under-represented patterns

Relative redundancy quantifies the whole pattern distribution by summing over all patterns "i". Here, we use two additional quantifiers that focus on special patterns. The *fraction of forbidden* patterns counts the number $\mathcal{N}$ of ordinal patterns [18] "i" that do not appear in the empirical distribution of size N (i.e. $n_i = 0$) and normalizes to the total number of available patterns:

$$f_0 = \frac{\mathcal{N}_{n_i=0}}{d!}. \tag{9}$$

If all $d!$ possible ordinal patterns are found at least once in the time series $f_0 = 0$ and $f_0 = 1 - 1/d! \approx 1$ if only one pattern is present. Application of the number and fraction of forbidden ordinal patterns to human intracranial EEG has been made in [16].

For some types of synthetic time series it can be shown analytically that certain ordinal patterns are indeed forbidden in the sense that their appearance is impossible, see e.g. the illustration for the logistic map with parameter $\alpha = 4$ and $d = 3$ in Fig. 1 of [33]. In contrast, real world time series are very often short and noise corrupted. Short time series may imply that the inequality Eq. (3) is not as good satisfied as it should and in consequence lead to random non-appearance of ordinal patterns mimicking forbidden patterns ("false forbidden patterns" [33,34]). On the other hand, noise contamination may randomly generate patterns that are strictly forbidden for the underlying deterministic dynamics. Thus, for sufficiently long and noise corrupted data, forbidden patterns will hardly ever be found. Finally, the probabilities of the ordinal patterns "i" are not necessarily uniformly distributed. For example, in low-pass filtered random time series ("colored noise") monotonic ordinal patterns may appear more frequently than oscillatory patterns. Rather than nonlinear determinism the reason is that the auto-correlation time is positive. To account for these effects we complement the search for strictly forbidden patterns by a search for patterns that appear significantly more rarely than in surrogate time series.

We generate a set of N_{AAFT} independent amplitude adjusted Fourier transform (AAFT) based surrogate time series [35,36]. They are phase randomized copies of the original time series that conserve the amplitude distribution exactly and approximate the Fourier spectrum. Specifically, any potential nonlinear determinism of the original time series that goes beyond effects of a finite auto-correlation function is destroyed. However, the influence of the finite length L of the observed time series and the power spectrum (especially $T_{\min}$) on the pattern frequencies n_i is supposed to be identical for the original data and the set of AAFT surrogates. Thus, the empirical null distribution of ordinal patterns "i" is sampled by

$$p_i = \frac{1}{N_{\mathrm{AAFT}}} \sum_{s=1}^{N_{\mathrm{AAFT}}} \frac{n_i^{(s)}}{N}, \tag{10}$$

where $n_i^{(s)}$ is the frequency of pattern "i" in surrogate s. This empirical construction is especially important in situations where the power spectrum and the auto-correlation function of the analyzed signals changes dynamically, as is typically the case for EEG during and after epileptic seizures.

Although the probabilities p_i of different ordinal patterns are not at all independent, it is legitimate to assume that under the null hypothesis of the AAFT surrogates the frequency n_i of a particular pattern "i" should follow a binomial distribution with parameters N (sample size) and p_i (probability). Examples of the normalized binomial distributions $P_i^{\mathrm{bino}}(n_i) = p^{\mathrm{bino}}(n_i|N,p_i)/p^{\mathrm{bino}}(n_i^{\max}|N,p_i)$ are shown in Fig. 2 for different N and p_i. Mean $\langle n_i \rangle = Np_i$, mode $n_i^{\max} = \lfloor (N+1)p_i \rfloor$, standard deviation $\mathrm{SD}_i = \sqrt{Np_i(1-p_i)}$ and skewness $(1-2p_i)/\sqrt{Np_i(1-p_i)}$ of this distribution depend on N and p_i. To quantify how "surprising" an empirical observation of pattern frequency n_i is for the given parameters we use $1 - P_i^{\mathrm{bino}}(n_i)$. The red shaded bars in Fig. 2 illustrate that non-observation of pattern "i" is much less expected in panel a than in panels b or c. Notwithstanding, in the fraction of forbidden patterns of Eq. (9) all situations would be counted equally (grey bars).

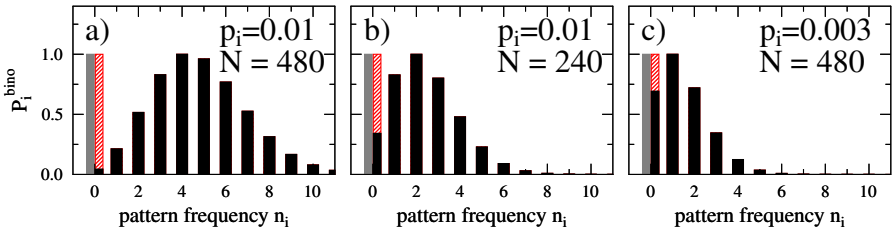

Fig. 2. Normalized binomial pattern frequency distribution P_i^{bino} for different pattern probabilities p_i and sample sizes N. a) mode of the binomial distribution $n_i^{\max} = 4$, b) $n_i^{\max} = 2$, c) $n_i^{\max} = 1$. The red shaded bars indicate the weight findings $n_i = 0$ would be given in the fraction of under-represented patterns, whereas the grey bar is the same for the fraction of forbidden patterns.

In contrast, we here introduce the *fraction of under-represented patterns* by

$$f_< = \frac{\sum_{i=1}^{d!} \sum_{n_i < n_i^{\max}} (1 - P_i^{\text{bino}}(n_i))}{\sum_{i=1}^{d!} (1 - P_i^{\text{bino}}(0))}. \tag{11}$$

The numerator sums up all ordinal patterns with empirical frequencies $n_i < n_i^{\max}$ (i.e. all patterns that appear less frequent than expected by the mode of the binomial distribution) and weights with the "surprise" $1 - P_i^{\text{bino}}(n_i)$ of finding n_i. The denominator normalizes to the maximal "surprise" that can be gained in all $d!$ ordinal patterns. If all empirical pattern frequencies n_i are close to their expectation $n_i^{\max}$ the fraction of under-represented patterns is positive but small $f_< \gtrsim 0$. In contrast, when only one pattern is found in the time series and all other patterns are under-represented we have $f_< \lesssim 1$. In the limit where $\langle n_i \rangle \gg 1$ (i.e. none of the patterns is rare in the surrogates) and $\text{SD}_i \ll \langle n_i \rangle$ (i.e. the frequency distribution expected from the surrogates is narrow) for all ordinal patterns "i" we have $f_< \to f_0$. This represents a situation where the grey and red shaded bars in Fig. 2 are (almost) equally long.

3 Simulations using the logistic map

To systematically explore the behavior of the above defined measures in a tunable setting we used the fully deterministic *logistic map* (see e.g. [37]), whose dynamics is given by the recurrence relation:

$$x_{t+1} = \alpha\, x_t(1 - x_t) \quad \in [0, 1]. \tag{12}$$

For most parameters $\alpha \gtrsim 3.57$ it exhibits chaotic behavior. We chose $\alpha = 3.92$ for our simulations to have a broad distribution of accessible amplitudes x and ignored the first 100 iterations to account for the possibility of transients.

The power spectrum of the logistic map may become very broad (almost white noise for our choice $\alpha = 3.92$). In contrast, the power of background EEG decays like $P(f) \sim f^{-\nu}$ with $1 \lesssim \nu \lesssim 2$ [38]. To approximate this dominance of low frequencies very crudely, we low-pass filtered x with a Butterworth filter with cutoff frequency $f_{\text{low}} = f_{\text{Nyquist}}/2 = f_{\text{sample}}/4$ and (very low) filter order one. This filtering leaves the time series fully deterministic and is denoted by the operator $\text{L}(\cdot)$ in the sequel.

To study the mixing of fully deterministic processes with filtered random processes (whose reminiscent of determinism is entirely due to the power spectrum, i.e. finite auto-correlation time), the dynamics x of eq. (12) was mixed with AAFT surrogates according to the rule

$$X = \rho \cdot \mathrm{N}(\mathrm{L}(x)) + (1-\rho) \cdot \mathrm{AAFT}(\mathrm{N}(\mathrm{L}(x))). \tag{13}$$

Here, the operator AAFT$(\cdot)$ generates AAFT surrogates and $0 \leq \rho \leq 1$ is the mixing parameter. The operator N$(\cdot)$ denotes signal normalization to zero mean and unit variance and guarantees that the signals X are normalized by construction. To mix the fully deterministic signal x and the non-deterministic surrogate signals with predefined signal-to-noise ratio (SNR) $s > 0$ we chose

$$\rho = \rho(s) = \begin{cases} 1/2 & \text{if} \quad s = 1 \\ \frac{s-\sqrt{s}}{s-1} & \text{otherwise.} \end{cases} \tag{14}$$

To test the sensitivity of the measures $M \in \{r, f_0, f_<\}$ for deterministic dynamics we scanned the parameter space in the region $0.25 \leq s \leq 16$, $d = 3, \ldots, 7$, $\tau = 1, 2, 3$ and SSR $= 2, \ldots, 5$. To test the null hypothesis that determinism in the time series X of Eq. (13) is significantly larger than in surrogate time series with (approximately) the same auto-correlation function we estimated parametric p-values as follows. From X a set of $N_{\mathrm{AAFT}} = 10$ AAFT surrogates was generated and the measures M were calculated for the original time series as well as for the surrogates. The percentile of the value obtained for X was estimated under the assumption of a Gaussian distribution for the surrogate results. $N_{\mathrm{ens}} = 10$ independent realizations of X were generated and the procedure was repeated. We here report mean values for M and p.

For any of the measures M we calculated the SNR contrast

$$\sigma_M = \left| \frac{M_{s=16} - M_{s=0.25}}{\langle M \rangle_s} \right| \tag{15}$$

and the order contrast

$$\delta_M = \left| \frac{M_{d=7} - M_{d=3}}{\langle M \rangle_d} \right| \tag{16}$$

to quantify the relative variation with s and d. An optimal measure should combine high SNR contrast σ (i.e. sensitive differentiation between noise dominated and determinism dominated time series) with low order contrast δ (i.e. small dependence of the results on the free parameter d). At the same time it should be monotonic in s and sensitive to determinism already for small SNR and SSR (i.e. the null hypothesis that the time series is a filtered random process should be rejected already for small parameter values).

Results of our parameter scan are shown in Fig. 3 for SSR $= 4$ and delay $\tau = 1$. The top row are the estimates for relative redundancy r (left column), the fraction of forbidden patterns f_0 (middle column) and the fraction of under-represented patterns $f_<$ (right column). The bottom row shows the negative logarithm $-\log_{10}(p)$ of the parametric p-value for differences to AAFT surrogate time series. As would be expected, signal determinism is best detected for large SNR s and large pattern order d. For the used model data the fraction of under-represented patterns has the largest area of sensitivity to deterministic structures. Except for $d \leq 4$ the fraction of under-represented patterns $f_<$ has largest SNR contrast σ. The order contrast δ of $f_<$ is larger than for r but considerably smaller than for f_0.

By showing means and standard deviations near the borders of sensitivity, Fig. 4 gives an overview of the reliability of the measures for $N_{\mathrm{ens}} = 10$ independent realizations of the dynamics Eq. (13). For $d = 5$, $\tau = 1$ and SSR=4 reliable detection

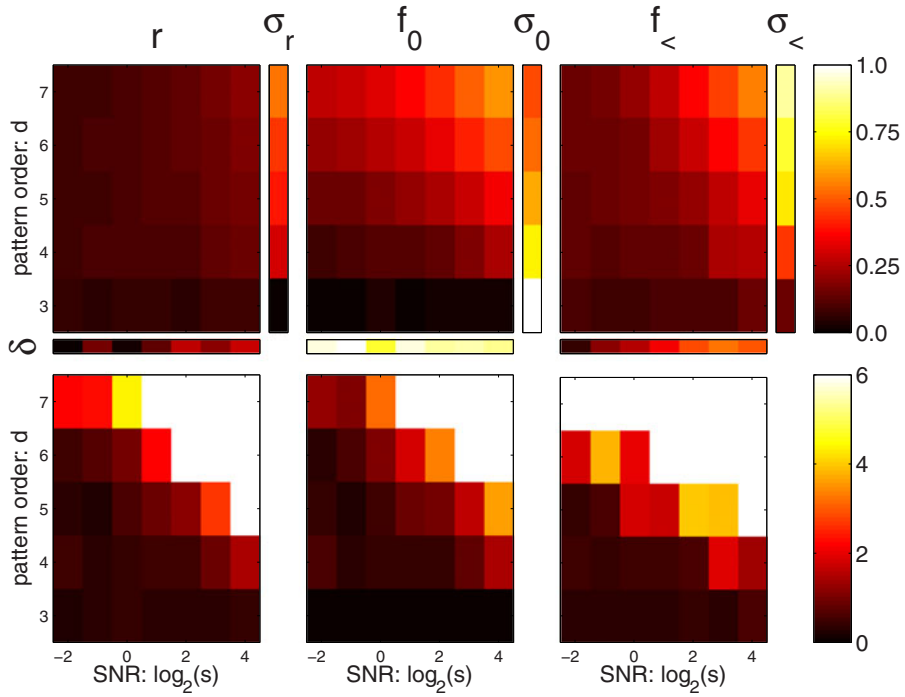

Fig. 3. Dependence of scalar quantifiers for pattern distributions on SNR s and pattern order d. Top row: quantifiers M and corresponding contrasts σ (vertical) and δ (horizontal). Contrasts are normalized to linearly fill the whole range between the largest and the smallest contrast to fit into the same color range. Bottom row: parametric significance $-\log_{10}(p)$ for compatibility with $N_{\mathrm{AAFT}} = 10$ AAFT surrogates. Fixed parameters are SSR $= 4$ and delay $\tau = 1$. Means of M and p are estimated over $N_{\mathrm{ens}} = 10$ independent realizations.

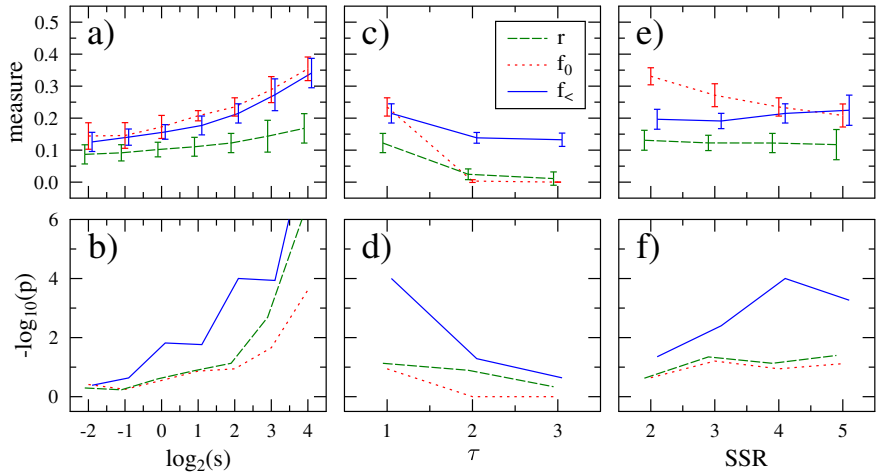

Fig. 4. Dependence of the determinism measures on SNR s (left), delay τ (middle) and SSR (right). Statistics (mean and standard deviation) is shown for $N_{\mathrm{ens}} = 10$ independent repetitions. Except the variable ones, parameters are $\log_2(s) = 2$, $d = 5$, $\tau = 1$ and SSR $= 4$. Significances were estimated parametrically with respect to $N_{\mathrm{AAFT}} = 10$ AAFT surrogates. For better visibility the curves were slightly shifted along the x-axis.

of determinism in time series becomes possible when the signal variance exceeds the noise variance by a factor larger than 2 (i.e. for $\log_2(s) \gtrsim 1$, see panel b). The significances of all three measures reduce with the delay τ (panel d). This observation reflects the fact that chaotic dynamics like the one of Eq. (12) are fully deterministic and therefore predictable on short time scales. In contrast, long-term prediction is impossible, thus chaotic time series appear more random if studied with larger delay.

4 Application to EEG of epilepsy patients

From our applications to real world data we show results for different types of EEG recordings from two epilepsy patients. Both suffered from epileptic seizures starting in the lateral part of the left temporal lobe. The seizures could not be controlled by one or a combination of several anti-seizure drugs. Therefore, the patients decided to undergo epilepsy surgery.

Patient 1 is a 19 year old female who suffered from seizures for 16 years. Structural magnetic resonance imaging (MRI) showed sclerosis of the left hippocampus. Patient 2 is a 26 year old male with normal appearing structural MRI. Epilepsy history was for the last 20 years. Both patients have become seizure free after surgery for more than one and more than two and a half years, respectively. This implies that the brain tissue responsible for seizure generation was successfully resected or that the epileptic network was successfully altered by the surgery. We can use this information to study the properties of the EEG signals generated by the resected brain areas and contrast them to signals originating from other brain areas.

During their pre-surgical work-up in our institutions both patients have received long-term EEG recording with scalp and intracranial electrodes and simultaneous EEG-fMRI. Electrode implantation and epilepsy surgery were performed completely independent from the present retrospective study, which was approved by the Ethics Comitee of the Kanton of Bern. Patients have signed informed consent that imaging and EEG data might be used for research purposes.

4.1 Intracranial EEG

If long-term scalp EEG recordings and structural MRI findings are not sufficiently concordant, electrodes can be implanted directly inside the brain and intracranial EEG (iEEG) is recorded, see e.g. [7,26]. These signals have much higher SNR and better spatial resolution. Routinely, seizures occuring during long-term iEEG recordings are used for visual identification of the seizure onset zone (SOZ) and seizure propagation pathways. Here, we present results from qEEG analysis based on ordinal patterns.

Details of the data acquisition and pre-processing are given in [16,39]. iEEG was recorded with 42 and 56 channels in patients 1 and 2, respectively, referenced to the median of all channels and filtered in $0.5\text{Hz} < f < 150\text{Hz}$ before analysis. Ordinal pattern distributions were generated from data segments of length $L = 1024$ (2 seconds after down-sampling), which were shifted over the data set with 1 second displacement. Pattern order and delay were $d = 5$ and $\tau = 1$, respectively. With these parameters the inequalities of Eqs. (3) to (5) are satisfied: $l = d = 9.8\,\text{ms}$, $T_{\min} = 6.7\,\text{ms}$, $\tau = 2.0\,\text{ms}$ and $N/d! = 8.5$.

Fig. 5 shows r (top), f_0 (middle) and $f_<$ (bottom) for an iEEG segment of patient 1 containing a focal onset seizure. During the seizure (start at $t = 0$, duration 4.5 minutes) all three measures exhibit similar dynamics. The most prominent increases are observed 30 seconds after visual seizure onset in channels 13–18 (depth

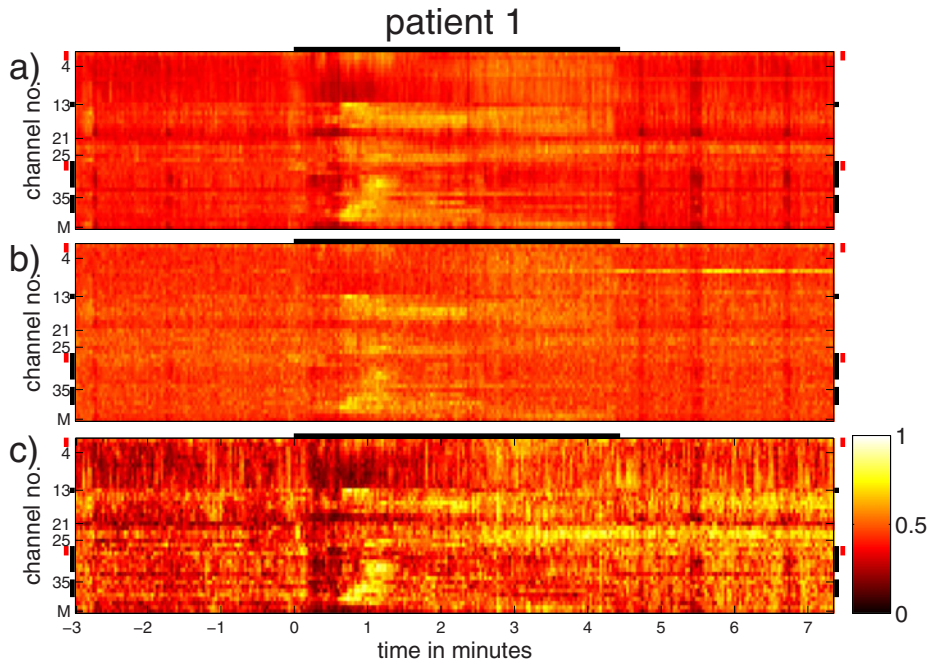

Fig. 5. Spatio-temporal evolution of the determinism measures during a focal onset seizure of patient 1 observed with intracranial EEG. a) relative redundancy r, b) fraction of forbidden patterns f_0, c) fraction of under-represented patterns $f_<$. The black horizontal bar on the top of the panels marks the seizure duration according to visual inspection of the raw iEEG. The vertical bars at the left and right panel margins indicate iEEG channels recording from tissue that was surgically removed (black) or contributed to the SOZ (red), respectively.

electrode implanted into the lateral left temporal lobe) and 30–39 (strip electrodes covering parts of the left temporal pole and the left middle temporal gyrus). The spatial contrast is largest for $f_<$, especially in the pre-seizure and post-seizure time period.

In this patient high-resolution T1-weighted post-operative MRI was co-registered with computed tomography (CT) of the head with implanted iEEG electrodes. This revealed that the iEEG channels 13, 27–32 and 35–38 recorded from brain tissue whose resection led to good outcome. Visual analysis of the iEEG by an experienced epileptologist (K.S.) revealed that the seizure onset zone (SOZ) of this particular seizure was in channels 1, 2 and 27, 28. The mean evolution of the determinism measures for the tissue that was later resected, the SOZ and all other channels are contrasted in Fig. 6. Before seizure we found intermittent time periods of significantly larger determinism ($p < 0.01$ in a t-test) in the resection area as compared to the remaining channels. Relative redundancy r (panel a) and the fraction of under-represented patterns $f_<$ (panel e) detected longer periods of increased determinism than the fraction of forbidden patterns f_0 (panel c). After approximately one minute of seizure evolution the determinism in the resected area exhibited a pronounced maximum, which, however, reached significance in $f_<$ only. In the second half of the seizure determinism was significantly reduced in the resected channels with the most pronounced decrease for r. Differences between the SOZ and the remaining channels were significant only for a short time near seizure onset (panels b and d). While $f_<$ did not detect significant differences, relative redundancy r found significantly increased determinism of the SOZ in the first seconds of the seizure.

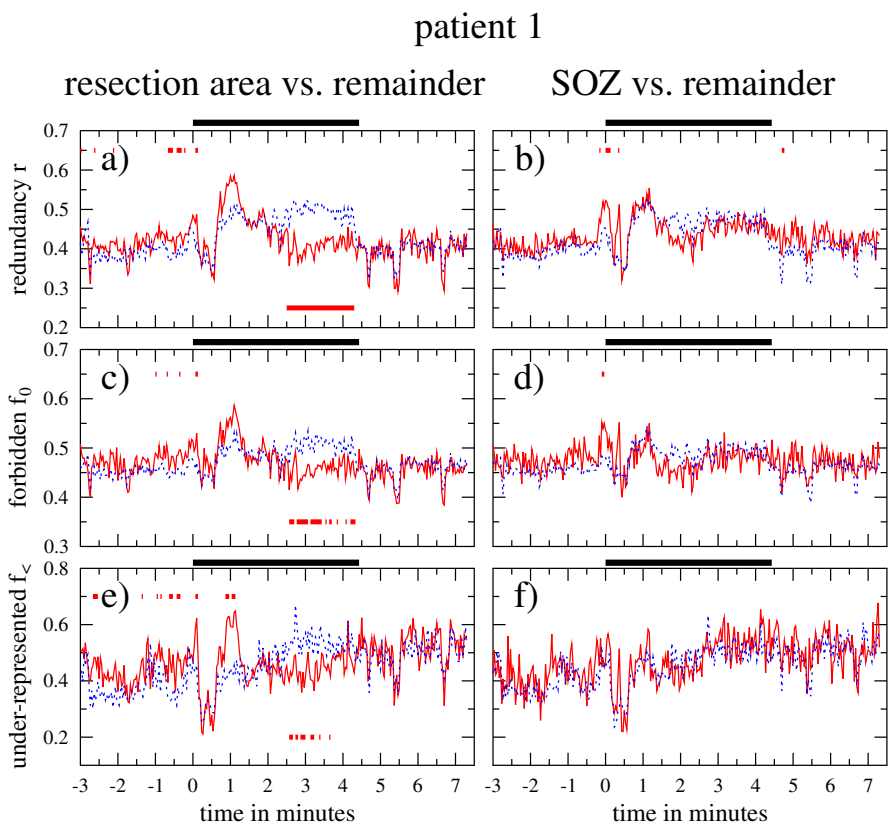

Fig. 6. Evolution of the scalar quantifiers during a focal onset seizure of patient 1 observed with intracranial EEG. Means are calculated over the resected contacts (left column, red line) or the SOZ (right column, red line) and the remainder (blue dashed in all panels). Periods where the red average is significantly larger (smaller) than the blue on significance level $p < 0.01$ (t-test) are indicated by red bars in the upper (lower) part of the panels. The black horizontal bar on the top of the panels marks the seizure duration according to visual inspection of the raw iEEG.

In patient 2 high-resolution T1-weighted post-operative MRI was not available and co-registration with CT was not possible. Instead we visually assessed the iEEG channels that were recording from the SOZ (ch. 6 and 7, marked by red bars on the margins of Fig. 7(a)) and the channels that were most likely resected during surgery (ch. 1–8, marked by grey bars on the margins of Fig. 7(a)). We focus the presentation of the results for this patient in Fig. 7 on the fraction of under-represented patterns. During seizure $f_<$ underwent a reorganization with pronounced maximum after one minute of seizure evolution. As in patient 1 increased determinism was significant in the channels that were presumably resected later on, while for the SOZ it was not. A difference between the two patients was that here we found smaller determinism of the resected brain areas before and after seizure.

4.2 Simultaneous EEG-fMRI

The good SNR and high spatial resolution of iEEG comes at the price of reduced brain coverage. Thus, previous information and hypotheses are necessary for electrode

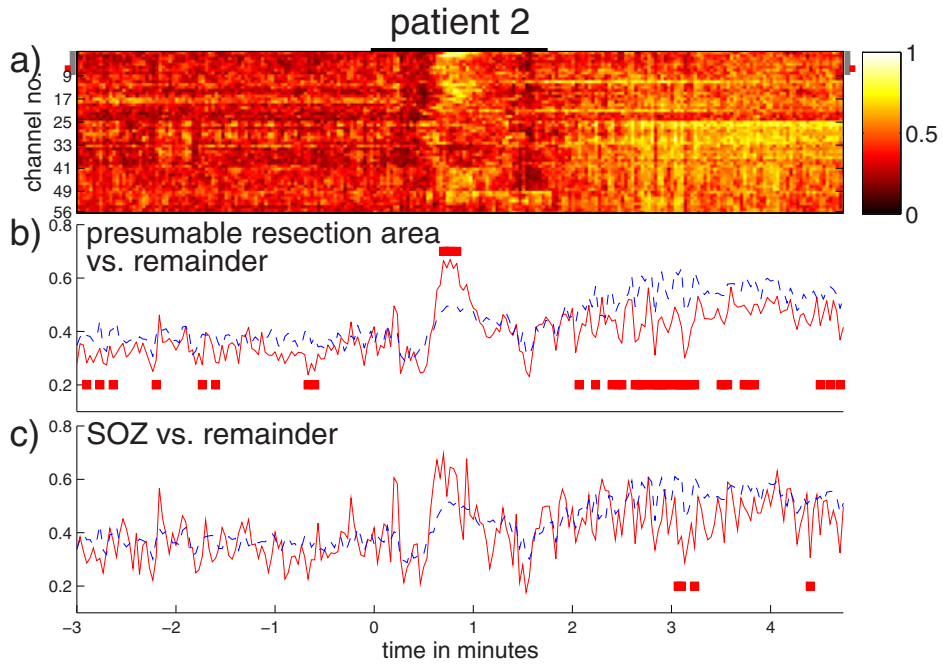

Fig. 7. Spatio-temporal evolution of the fraction of under-represented patterns $f_<$ during a focal onset seizure of patient 2 observed with intracranial EEG. Colors and graph elements have the same meaning as in Figs. 5 and 6.

implantation. Besides classic long-term scalp EEG and structural MRI one possibility is combined registration of scalp EEG and functional MRI (fMRI), see e.g. [27–29]. This non-invasive technique allows whole head coverage and combines the excellent temporal resolution of EEG with the high spatial resolution of fMRI. This way one tries to overcome the limited spatial resolution of scalp EEG and the limited temporal resolution of fMRI.

Details of our approach to EEG-fMRI can be found in [40–42]. In short, we used a 3 Tesla Siemens Magnetom Trio™ TIM MR Scanner (Erlangen, Germany) for the MRI data acquisition. The blood oxygen level dependent (BOLD) data was acquired using a multi-slice single-shot T2*-weighted echo planar imaging sequence (EPI). In the first patient $L = 460$ functional volumes were measured spaced at repetition time TR = 1980 ms. For the second patient $L = 220$ volumes were acquired with TR = 4130 ms. The scalp EEG was recorded with 92 channels (plus two EOG and two ECG channels) on a MR compatible EEG cap. The signals were sampled at rate 5 kHz, filtered in the pass band $1\,\text{Hz} < f < 30\,\text{Hz}$ and down-sampled to 500 Hz sampling rate.

The EEG was decomposed into least dependent components using temporal independent component analysis (ICA) [43]. Based on the time courses, power spectra and spatial mapping of spikes one ICA factor that coded best for inter-ictal epileptic discharges (IEDs) was selected visually by experienced epileptologists (M.H., R.W.). After two alternative post-processing pipelines (see below) the EEG-ICA factors were convolved with a double gamma hemodynamic response function (HRF) and used as predictors in a general linear model (GLM) for the measured BOLD signals, see Fig. 8. Nuisance time series included the mean BOLD signals of white matter and cerebrospinal fluid as well as the motion correction parameters (three translations and three rotations). From the GLM parameter estimates of the EEG-ICA predictor and the

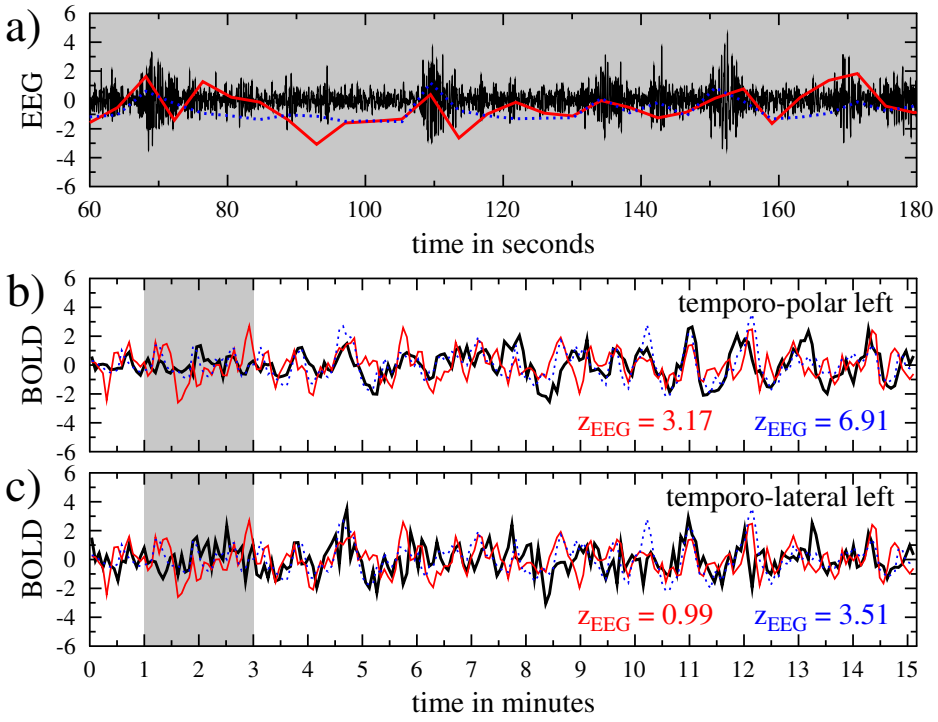

Fig. 8. Illustration of the EEG-fMRI data analysis at the example of patient 2. a) Two minutes of the visually selected EEG-ICA factor (black), post-processing by rectification (blue dotted) and fraction of under-represented patterns (red) in the selected factor; b) raw BOLD time series of a voxel in the temporal pole of the left hemisphere (black) and EEG-ICA predictors after convolution with the HRF: post-processing by standard rectification (dotted blue) and symbolic post-processing (red); c) same for a temporo-lateral voxel, where only the rectification post-processing has predictive power for the BOLD response. All time series were normalized to zero mean and unit variance in order to have the same scales on the y-axes. The grey shaded areas indicate the same segment of EEG-fMRI. z-scores quantify the explanatory power of the shown EEG predictor time series for the BOLD signals.

residual time series z-scores were estimated that quantify the explanatory power of the EEG activity for the BOLD signals.

The standard post-processing of the selected EEG-ICA factor consisted in signal rectification [40]. The absolute values of the time series were integrated over the repetition time TR of an EPI volume. Here, we contrast the rectification procedure with calculation of the fraction of under-represented patterns $f_<$ with parameters $d = 5$ and $\tau = 5$ over the time span TR. With these parameters the inequalities of Eqs. (3) to (5) are satisfied: $l = 42\,\mathrm{ms}$, $T_{\min} = 40\,\mathrm{ms}$, $\tau = 2\,\mathrm{ms}$ and $N/d! = 8.2$.

Our results for patient 1 are presented in Fig. 9, projected onto high-resolution post-operative MRI. The EEG-ICA predictor with rectification post-processing (cool colors) shows extended BOLD signal correlates in the lateral and medial temporal lobe (upper row), as well as parts of the occipital lobe and the insula (lower row), all in the left hemisphere. Some artifactual (noise) correlates are visible in the nasal cavities bilaterally. In contrast, with ordinal pattern post-processing (hot colors) the same EEG-ICA factor shows highly localized BOLD signal correlates predominantly in the hippocampus of the left medial temporal lobe, few correlates in the left insula and one additional cluster of activation in the left thalamus (lower row, rightmost

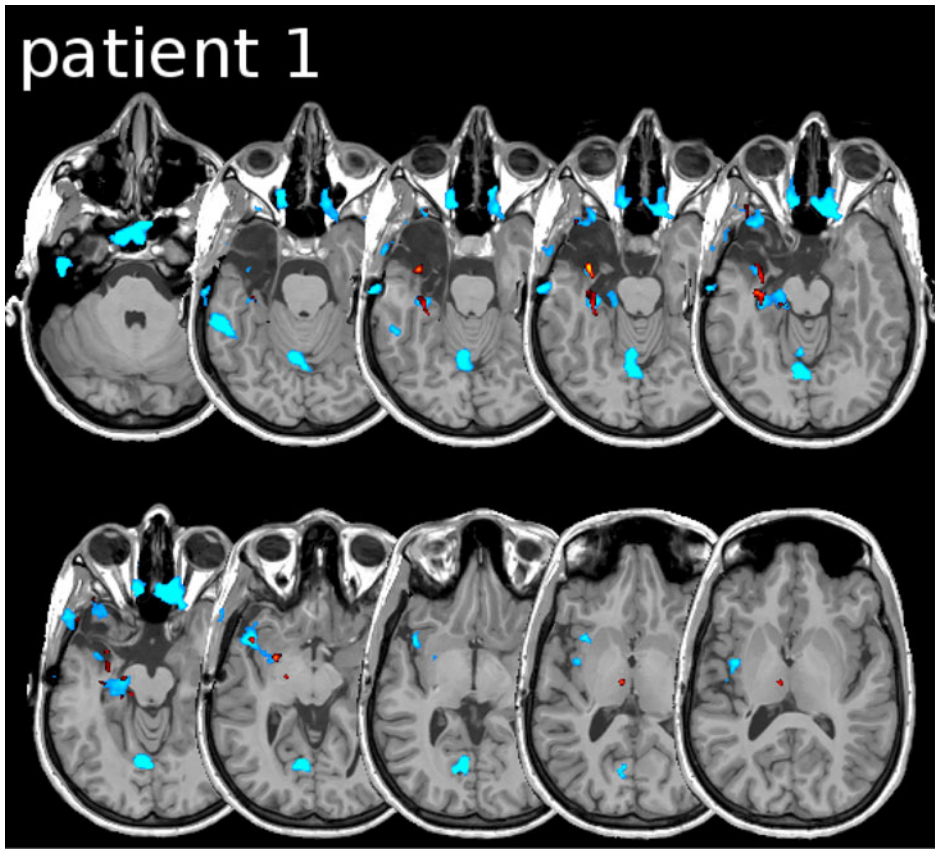

Fig. 9. Localization of EEG-ICA derived predictors in the fMRI. The activation maps are projected onto a post-operative high-resolution structural MRI. Images are in neurological orientation, i.e. the right side of the image corresponds to the right side of the brain. The resected part of the left temporal lobe is reflected by low signal intensities in the background images. Both color scales for activation z-scores are in the same range $3 \leq z \leq 5$. The cold color scale (blue-green) represents the correlates to the rectified predictor, while the hot color scale (red-yellow) is the predictor based on the fraction of under-represented patterns.

slice). Noise correlates are markedly reduced for this post-processing variant. Note that the cluster of strongest correlation is clearly located inside the resected area (low signal intensities of the background image). The involvement of the thalamus is in line with previous studies that show marked metabolic and structural abnormalities of this region in patients with temporal lobe epilepsy [44,45].

Figure 10 summarizes the results for patient 2 using the same color code as above. Again, the BOLD response to rectification post-processing is much more extended than to ordinal pattern post-processing, covering the anterior, lateral and medial temporal lobe of the left hemisphere, as well as parts of the left insula and the right occipital lobe. Although the ordinal pattern post-processing shows more widespread correlates than in patient 1, the largest clusters are clearly located in the anterior temporal lobe and the hippocampus. No high-resolution post-operative scans were available to directly assess the spatial relationship between BOLD correlates and tissue resection in patient 2. Nevertheless, visual inspection revealed that all anterior clusters of the ordinal pattern post-processed predictor had been removed during surgery.

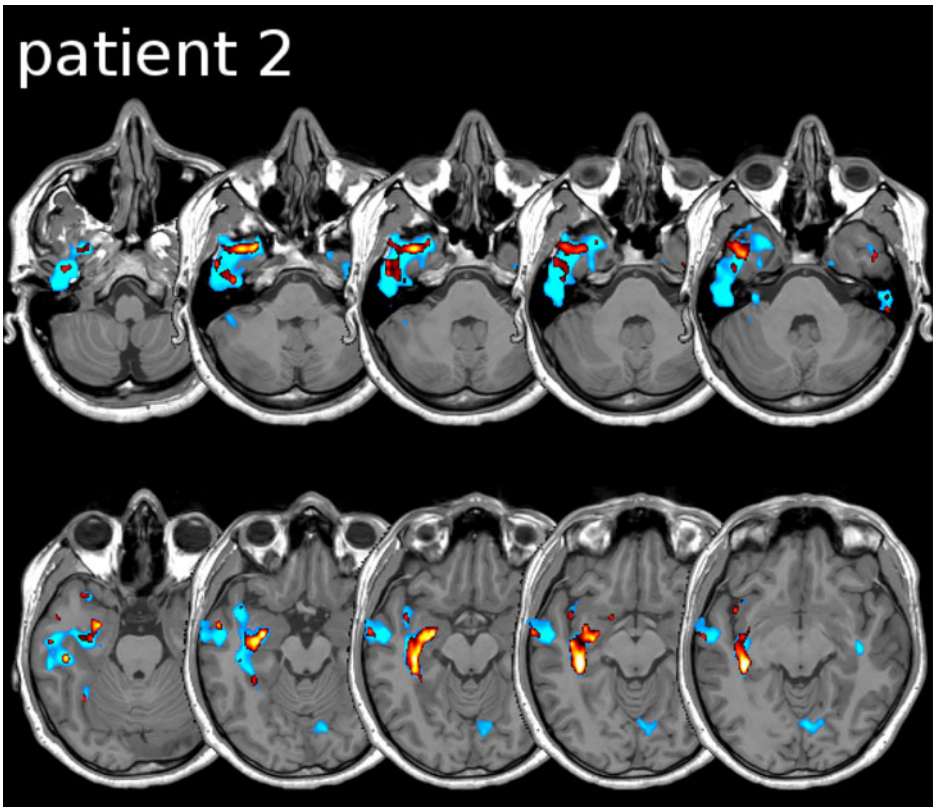

Fig. 10. Same as Fig. 9 but for patient 2. As post-operative high-resolution structural MRI was not available the activation maps are projected onto the pre-operative image.

5 Discussion

In our contribution we have introduced the fraction of under-represented patterns $f_<$ in Eq. (11), which offers an advantage over the fraction of forbidden patterns f_0 in certain cases. The reason is that the chance of not finding one or several ordinal patterns depends on the pattern probability p_i and the sample size N, see Fig. 2. By its construction $f_<$ is more appropriate for signals with dominant low frequencies and less vulnerable to noise and small SSR, see Figs. 3 and 4.

Unfortunately, a simple model producing non-random, chaotic deterministic time series x with realistic power spectrum for EEG does not exist. This led us to the workaround using low-pass filtered deterministic time series generated from the logistic map in Eq. (13). For our parameter choice $\alpha = 3.92$ and without the filtering step the empirical probabilities p_i would approximate $1/d!$ closely for all ordinal patterns "i", a situation that is not realistic for EEG time series. Then $\langle n_i \rangle = \mathrm{SSR}$, $\mathrm{SD}_i \approx \sqrt{\mathrm{SSR}}$ and except for very small SSR the binomial distribution $P_i^{\mathrm{bino}}(n)$ would resemble the situation depicted in Fig. 2(a), where the advantage of $f_<$ over f_0 is expected to be minimal.

Despite considerable overall similarities, differences between the determinism measures r, f_0 and $f_<$ are present for peri-ictal intracranial EEG. In patient 1 the fraction of under-represented patterns had largest spatial (Fig. 5) and temporal contrast (Fig. 6). In both patients we found significantly larger determinism in the resected brain tissue approximately one minute after seizure onset (Figs. 6(e) and 7(b)). In

contrast, no significant differences were found for the visually determined SOZ of these particular seizures (Figs. 6(f) and 7(c)). If this observation generalizes to other patients, ordinal pattern analysis of iEEG could potentially provide useful complementary information for planning of epilepsy surgery. Deeper investigation in larger patient groups remains necessary.

We found that analyzing simultaneous EEG-fMRI data the BOLD responses to EEG-ICA predictors, encompassed the brain region whose resection led to seizure freedom. Interestingly, as compared to the standard procedure of predictor rectification, the calculation of $f_<$ reduced the spatial extension of activations considerably (Figs. 9 and 10). Of note, increasing the spatial localizing power of EEG-fMRI could prove very useful in the clinical setting, e.g. for guiding iEEG implantation or even determining the extent of resection targets [29]. Comparing resected areas with symbolic BOLD correlates could also be used as a quality control measure, especially in patients who have not become seizure free after surgery.

Although a proper assessment of spatial sensitivity and specificity of the two alternative post-processing procedures is still lacking, one might speculate that signal determinism is the relevant feature of IED associated ICA factors in the EEG of epilepsy patients. While rectified predictors contain this information, the ordinal pattern post-processing explicitly focuses on this property. It remains to investigate systematically, whether ordinal pattern analysis of EEG-ICA predictors may provide more objective selection criteria than the current visual analysis.

This work was funded by Schweizerischer Nationalfonds, Switzerland (grants 33CM30-140332 and 33CM30-124089). The authors report no conflict of interest relevant to this article.

References

1. H.M. de Boer, M. Mula, J.W. Sander, Epilepsy Behav. **12**, 540 (2008)
2. R.S. Fisher, W. van Emde Boas, W. Blume, C. Elger, P. Genton, P. Lee, J.J. Engel, Epilepsia **46**, 470 (2005)
3. F. Mormann, R.G. Andrzejak, C.E. Elger, K. Lehnertz, Brain **130**, 314 (2007)
4. R.G. Andrzejak, D. Chicharro, C.E. Elger, F. Mormann, Clin. Neurophysiol. **120**, 1465 (2009)
5. K. Lin, S.R. Benbadis, Expert Rev. Neurother. **9**, 781 (2009)
6. C.E. Elger, D. Schmidt, Epilepsy Behav. **12**, 501 (2008)
7. H.O. Lüders, *Textbook of Epilepsy Surgery* (Informa Healthcare, London, 2008)
8. P. Gloor, in *Current Concepts in Clinical Neurophysiology*, edited by D.N.J. Van Duyn and H. Donker, A.C. Van Huffelen (NV Drukker Trio, The Hague, The Netherlands, 1977), p. 9
9. C.J. Keller, W. Truccolo, J.T. Gale, E. Eskandar, T. Thesen, C. Carlson, O. Devinsky, R. Kuzniecky, W.K. Doyle, J.R. Madsen, et al., Brain **133**, 1668 (2010)
10. A. Galka, *Topics in Nonlinear Time Series Analysis: With Implications for EEG Analysis* (World Scientific Publishing, Singapore, 2000)
11. E. Pereda, R. Quian Quiroga, J. Bhattacharya, Prog. Neurobiol. **77**, 1 (2005)
12. C. Stam, Clin. Neurophysiol. **116**, 2266 (2005)
13. C. Rummel, R.G. Andrzejak, K. Schindler, Epileptologie **29**, 99 (2012)
14. P. Brockwell, R. Davis, *Time Series: Theory and Methods* (Springer, New York, 1987)
15. H. Kantz, T. Schreiber, *Nonlinear Time Series Analysis*, 2nd edn. (Cambridge University Press, Cambridge, 2004)
16. K. Schindler, H. Gast, L. Stieglitz, A. Stibal, M. Hauf, R. Wiest, L. Mariani, C. Rummel, Epilepsia **52**, 1771 (2011)
17. C. Masoller, O.A. Rosso, Philos. Trans. R. Soc. A **369**, 425 (2011)
18. J. Amigo, L. Kocarev, J. Szczepanski, Phys. Lett. A **355**, 27 (2006)

19. C. Bandt, B. Pompe, Phys. Rev. Lett. **88**, 174102 (2002)
20. K. Keller, H. Lauffer, Int. J. Bifur. Chaos **13**, 2657 (2003)
21. A. Groth, Phys. Rev. E **72**, 046220 (2005)
22. G. Ouyang, C. Dang, D. Richards, X. Li, Clin. Neurophysiol. **121**, 694 (2010)
23. G. Ouyang, X. Li, C. Dang, D. Richards, Phys. Rev. E **79**, 041146 (2009)
24. K. Schindler, H. Gast, M. Goodfellow, C. Rummel, Epilepsia **53**, 1658 (2012)
25. M. Zanin, L. Zunino, O.A. Rosso, D. Papo, Entropy **14**, 1553 (2012)
26. F. Rosenow, H. Lüders, Brain **124**, 1683 (2001)
27. J. Gotman, E. Kobayashi, A.P. Bagshaw, C.G. Bénar, F. Dubeau, J. Magn. Reson. Imag. **23**, 906 (2006)
28. P. Ritter, A. Villringer, Neurosci. Behav. Rev. **30**, 823 (2006)
29. M. Zijlmans, G. Huiskamp, M. Hersevoort, J.H. Seppenwoolde, A.C. van Huffelen, F.S. Leijten, Brain **130**, 2343 (2007)
30. O. Rosso, H. Larrondo, M. Martín, A. Plastino, M. Fuentes, Phys. Rev. Lett. **99**, 154102 (2007)
31. A. Kowalski, M. Martín, A. Plastino, O. Rosso, Physica D **233**, 21 (2007)
32. B. Frank, B. Pompe, U. Schneider, D. Hoyer, Med. Biol. Eng. Comput. **44**, 179 (2006)
33. J.M. Amigó, S. Zambrano, M.A.F. Sanjuán, Europhys. Lett. **79**, 50001 (2007)
34. J.M. Amigó, S. Zambrano, M.A.F. Sanjuán, Europhys. Lett. **83**, 60005 (2008)
35. J. Theiler, S. Eubank, A. Longtin, B. Galdrikian, J. Farmer, Physica D **58**, 77 (1992)
36. T. Schreiber, A. Schmitz, Physica D **142**, 346 (2000)
37. S.H. Strogatz, *Nonlinear Dynamics and Chaos* (Perseus Book Publishing, Cambridge, MA, 2000)
38. G. Buzsáki, *Rhythms of the Brain* (Oxford University Press, New York, 2006)
39. K. Schindler, F. Amor, H. Gast, M. Müller, A. Stibal, L. Mariani, C. Rummel, Epilepsy Res. **89**, 72 (2010)
40. K. Jann, R. Wiest, M. Hauf, K. Meyer, C. Boesch, J. Mathis, G. Schroth, T. Dierks, T. Koenig, NeuroImage **42**, 635 (2008)
41. M. Hauf, K. Jann, K. Schindler, O. Scheidegger, K. Meyer, C. Rummel, L. Mariani, T. Koenig, R. Wiest, Am. J. Neuroradiol. **33**, 1818 (2012)
42. M. Hauf, O. Scheidegger, C. Rummel, A. Rahman, R. Wiest, Epileptologie **29**, 90 (2012)
43. A. Delorme, S. Makeig, J. Neurosci. Meth. **134**, 9 (2004)
44. C. Juhász, F. Nagy, C. Watson, E.A. da Silva, O. Muzik, D.C. Chugani, J. Shah, H.T. Chugani, Neurology **53**, 2037 (1999)
45. S. Dreifuss, F.J. Vingerhoets, F. Lazeyras, S.G. Andino, L. Spinelli, J. Delavelle, M. Seeck, Neurology **57**, 1636 (2001)